

Corrosion and Carburization Behaviour of Ni- x Cr Binary Alloys in a High-Temperature Supercritical-Carbon Dioxide Environment

Gokul Obulan Subramanian¹ · Ho Jung Lee¹ · Sung Hwan Kim¹ · Changheui Jang¹ 

Received: 14 August 2017 / Revised: 12 October 2017 / Published online: 23 October 2017
© Springer Science+Business Media, LLC 2017

Abstract Pure Ni and Ni- x Cr ($x = 7, 14, 22$ and 27 wt%) binary alloys were exposed to supercritical-carbon dioxide environment at 600 °C and 20 MPa for 200 h. For pure Ni, a thick NiO layer was formed on the surface. Meanwhile, for Ni-7Cr alloy, an inner oxide layer consisted of rather irregular chromia and NiO was formed below the outer NiO layer. When Cr content was greater than 14% , a continuous chromia layer was formed, resulting in much lower weight gain and oxide thickness. However, amorphous carbon layers had developed along the oxide–matrix interface when chromia was formed. The presence of the carbon layer was explained in view of the high C activity corresponding to the low equilibrium oxygen potential of chromia.

Keywords Ni-based alloys · High-temperature corrosion · Carburization · Supercritical carbon dioxide

✉ Changheui Jang
chjang@kaist.ac.kr
Gokul Obulan Subramanian
gokul@kaist.ac.kr
Ho Jung Lee
leehojung@kaist.ac.kr
Sung Hwan Kim
sciencetom@kaist.ac.kr

¹ Korea Advanced Institute of Science and Technology, Daejeon 34141, Republic of Korea

Introduction

A supercritical- CO_2 (S- CO_2) Brayton cycle is considered as a promising power conversion system for nuclear [1–3], solar thermal [4], geothermal [5] and fossil fuel [6] power generation systems. A few advantages of S- CO_2 Brayton cycle over both the steam and gas turbine systems include the reduced compressive power requirement, higher thermal efficiency, much smaller components size and comparatively less material issues at high temperature [1, 2].

Recently, the corrosion and carburization behaviour of several Fe- and Ni-based alloys has been extensively investigated in high-temperature CO_2 and S- CO_2 environments [7–12]. Overall, Ni-based alloys showed better corrosion resistance than stainless steels because of the formation of stable and continuous chromia (Cr_2O_3) layer on the surface [10]. For austenitic stainless steels, discontinuous islands of carburized M_{23}C_6 regions were found below the oxide layer, which appeared to promote spallation of oxide layer after long-term exposure [9, 10]. Whereas, an amorphous C layer was observed at the interface between the chromia layer and underlying matrix for the Ni-based alloys exposed up to 1000 h at 550–650 °C (20 MPa) [11, 12]. Despite the presence of the C layer, carbide precipitates were not found in the matrix, and spallation of oxide layer was not observed. Nonetheless, the development of the amorphous C layer under the inner chromia was rather surprising, considering the presence of the continuous and seemingly protective chromia layer. Meanwhile, no such C layer was observed when pre-formed alumina layer was present on the surface [13].

In this regard, the role of oxide layers, especially a chromia layer, on the characteristics of the oxide layer and its subsequent impact on the carburization behaviour of Ni-based alloys need to be understood. Therefore, the objective of this study is to investigate the effect of Cr content in Ni-based binary alloys on the corrosion and carburization behaviour in high-temperature S- CO_2 condition, emphasizing the role of chromia layer on the carburization behaviour. For this, pure Ni and Ni- $x\text{Cr}$ binary alloys were prepared and exposed to S- CO_2 environment at 600 °C and 20 MPa for 200 h. The corrosion and carburization resistance were characterized by weight gain measurements and several analytical techniques. Finally, carburization resistance was discussed in view of the equilibrium oxygen partial pressure $(p\text{O}_2)_{\text{eq}}$ of the oxides formed on the Ni- $x\text{Cr}$ binary alloys.

Materials and Experimental

The pure Ni and Ni- $x\text{Cr}$ ($x = 7, 14, 22$ and 27 wt%) binary alloys were prepared by vacuum arc remelting using pure Ni and Cr metal scrap pieces with 99.995% purity. The chemical composition of the as-cast alloys was confirmed by inductively coupled plasma (ICP) analysis. The as-cast pure Ni showed a fully austenite microstructure with an ASTM grain size number of about 8.5. For the Ni- $x\text{Cr}$ binary alloys containing $\text{Cr} \geq 7\%$, grains were much coarser with an ASTM grain size number of about 2.5. All the materials were cut into coupon-type specimens with

12 mm in diameter and 1 mm in thickness. A hole of 1.5 mm in diameter was drilled at the upper part of the specimens for a hanging wire. The specimens were ground to 1200 grit finish and ultrasonically cleaned with ethanol before the corrosion test. The specimens were hung with a Pt wire of 0.5 mm diameter, separated with alumina spacers and kept in an alumina boat placed in the autoclave. An isothermal corrosion test was conducted at 600 °C and 20 MPa for 200 h in an S-CO₂ corrosion test facility by feeding a research-grade CO₂ gas (99.999% purity) to a high-pressure CO₂ pump. The oxygen partial pressure p_{O_2} was calculated as 1.23×10^{-7} atm [12]. The detailed description of experimental set-up and procedure could be found elsewhere [11].

After the tests, the weight gains of the specimens were measured using a microbalance (Mettler Toledo AT21 Comparator) with 0.001 mg resolution. To characterize the oxide layer and underlying microstructure in the Ni-xCr binary alloys, X-ray diffraction (XRD, Rigaku D/MAX-2500), transmission electron microscope (TEM, Titan cubed G2 60–300) equipped with energy dispersive spectroscopy (EDS) and secondary ion mass spectroscopy (SIMS, CAMECA IMS 7f) analyses were performed. The TEM specimens were taken from the corroded specimens using a focused ion beam (FIB, Helios Nanolab 450 F1). The equilibrium oxygen partial pressure $(p_{O_2})_{eq}$ of various oxides in contact with matrix of Ni-xCr binary alloys and carbide stability diagram were calculated using Thermo-Calc[®], a commercial thermodynamic software, to understand the carburization mechanism.

Results and Discussion

Corrosion Behaviour in S-CO₂ Environment

Figure 1 shows the measured weight gain and oxide thickness of pure Ni and Ni-xCr binary alloys exposed to S-CO₂ environment. Compared to pure Ni and Ni-7Cr,

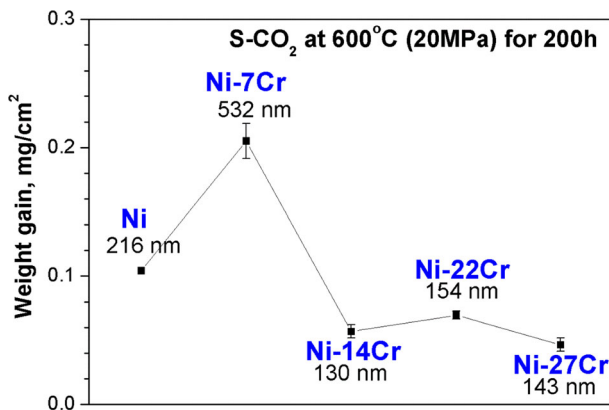


Fig. 1 Weight gains and oxide thickness of Ni-xCr binary alloys corroded in S-CO₂ at 600 °C (20 MPa) for 200 h

binary alloys containing at least 14% Cr showed better corrosion resistance with smaller weight gain and thinner oxide thickness. In addition, the corrosion resistance was about the same for the alloys with at least 14% Cr. On the other hand, the corrosion resistance of Ni-7Cr binary alloy was the worst among the tested alloys in terms of weight gain and oxide thickness. The large increase in weight gain for Ni-7Cr alloy compared to pure Ni could have been attributed to the oxidation of Cr present in the matrix. XRD results of the alloys exposed to S-CO₂ environment are shown in Fig. 2. For all tested alloys, the predominant peaks observed from XRD analysis can be attributed to the matrix, consistent with the thin oxide thickness shown in Fig. 1. Other than matrix peaks, only NiO peaks were observed for pure Ni, whereas minor chromia peaks as well as strong NiO peaks were shown for Ni-7Cr binary alloy. Meanwhile, only chromia peaks were observed for the alloys with at least 14% Cr. In addition, alloys with 14–27% Cr exhibited similar XRD results, suggesting the presence of similar oxide characteristics for these alloys. Overall, XRD results shown in Fig. 2 combined with weight gain results shown in Fig. 1 confirmed that the formation of the predominantly chromia layer showed better corrosion resistance in high-temperature S-CO₂ environment.

The detailed cross-sectional STEM-EDS analyses results of oxide layer and underlying matrix of the tested alloys are shown in Figs. 3, 4, 5 and 6. For pure Ni exposed to S-CO₂ environment, a rather uniform oxide layer was observed on the surface, which was identified as NiO based on EDS mapping and line scanning results (Fig. 3). It should be noted that the slight presence of Cr and C in the oxide layer can be attributed to the electronic noise evolved during the STEM-EDS line

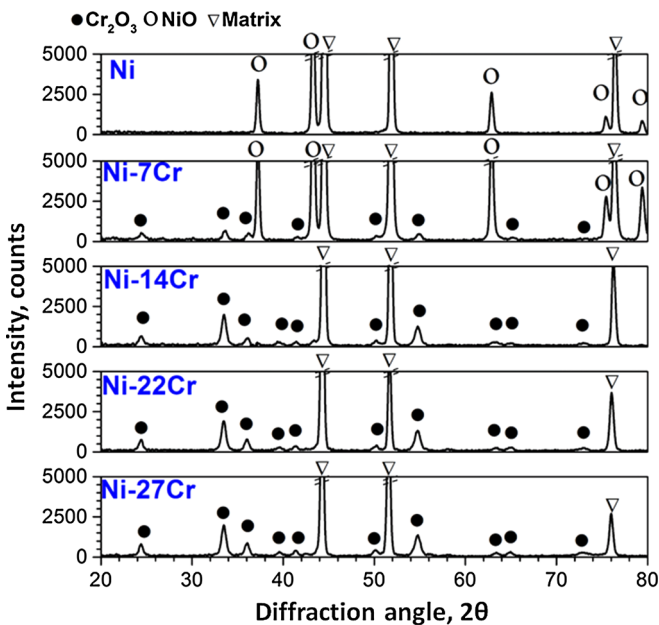


Fig. 2 XRD analysis results of Ni-*x*Cr binary alloys corroded in S-CO₂ at 600 °C (20 MPa) for 200 h

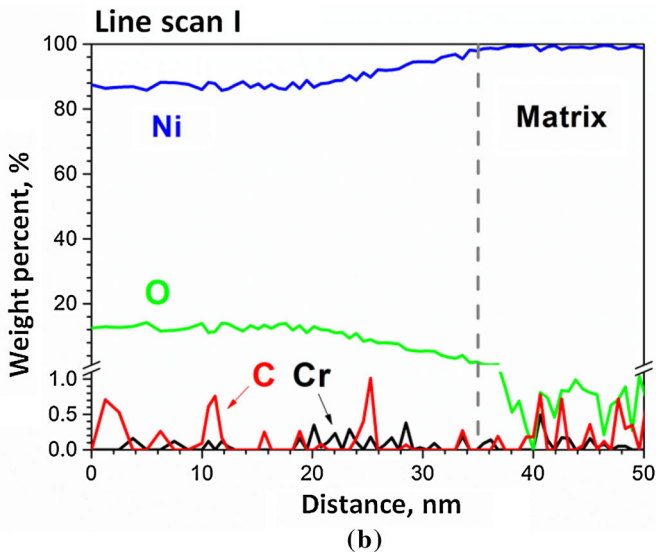
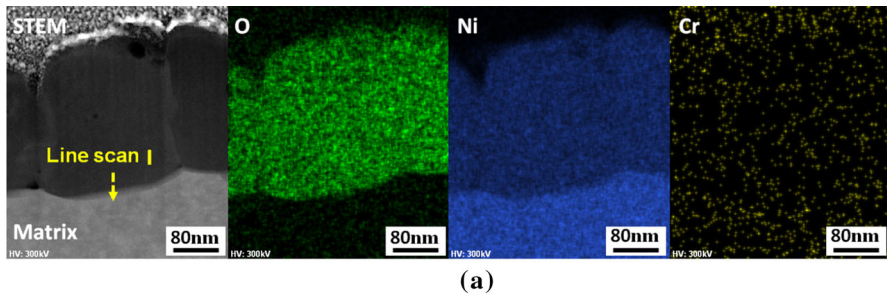
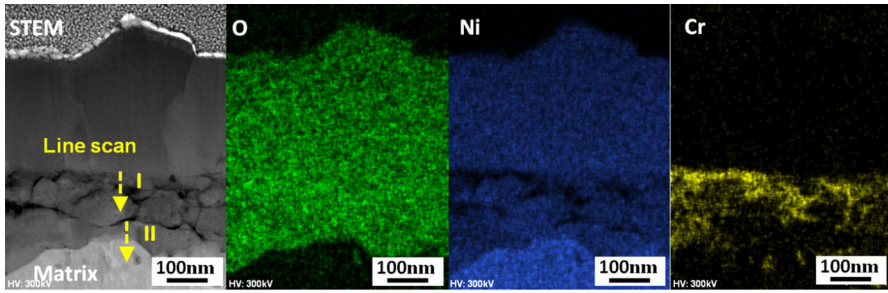


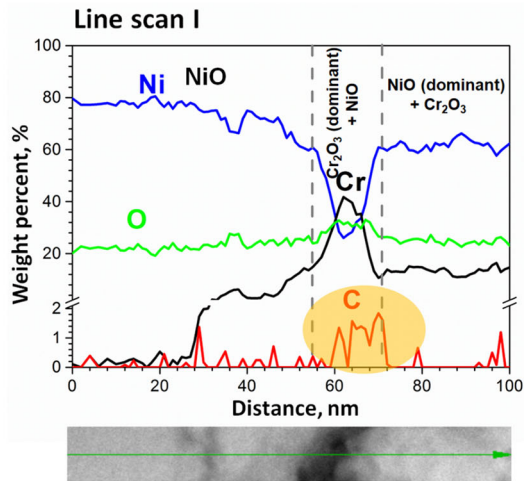
Fig. 3 TEM analyses results of oxide layer on pure Ni corroded in S-CO₂ at 600 °C (20 MPa) for 200 h. **a** Cross-sectional STEM micrograph and EDS mapping images and **b** line scan at the matrix–oxide interface

scan process since it had been confirmed that no Cr had been present in the pure Ni specimens by ICP analysis. Whereas, Ni-7Cr binary alloy showed a complex oxide structure consisted of outer uniform NiO layer and inner layer of a rather irregular Cr₂O₃ mixed with NiO (Fig. 4b, c). The formation of the rather complex oxide structure could be explained as follows. Initially, NiO would be formed on the surface due to small amount of Cr in the Ni-matrix insufficient to form the protective chromia. It was reported that for dilute Ni–Cr binary alloys oxidized at high temperature, the internal Cr₂O₃ and NiO would grow by either oxygen transport from NiO dissociation or through the short-circuit transport of oxidants from the atmosphere [14]. Meanwhile, the presence of amorphous C region around the internal chromia (Fig. 4d) suggests that carbonaceous species would have transported into the matrix to grow Cr₂O₃ and NiO internally.

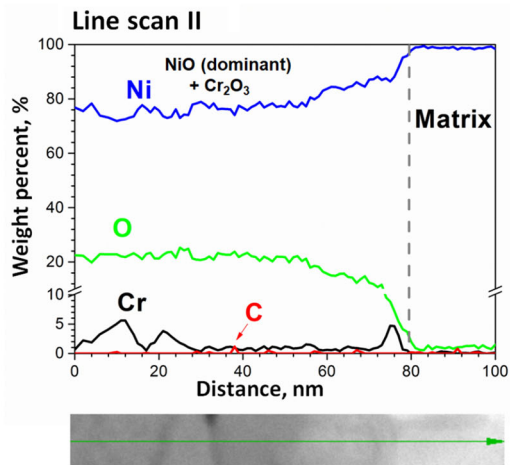
Meanwhile, EDS mapping results (Fig. 4a) showed that NiO and Cr₂O₃ were separately present in the inner layer without forming mixed NiCr₂O₄ oxides, which



(a)



(b)



(c)

Fig. 4 TEM analyses results of oxide layer on Ni-7Cr binary alloy corroded in S-CO₂ at 600 °C (20 MPa) for 200 h. **a** Cross-sectional STEM micrograph and EDS mapping images, **b** line scan I, **c** line scan II at the matrix–oxide interface and **d** STEM micrograph, HRTEM micrograph and EDS mapping of amorphous C region

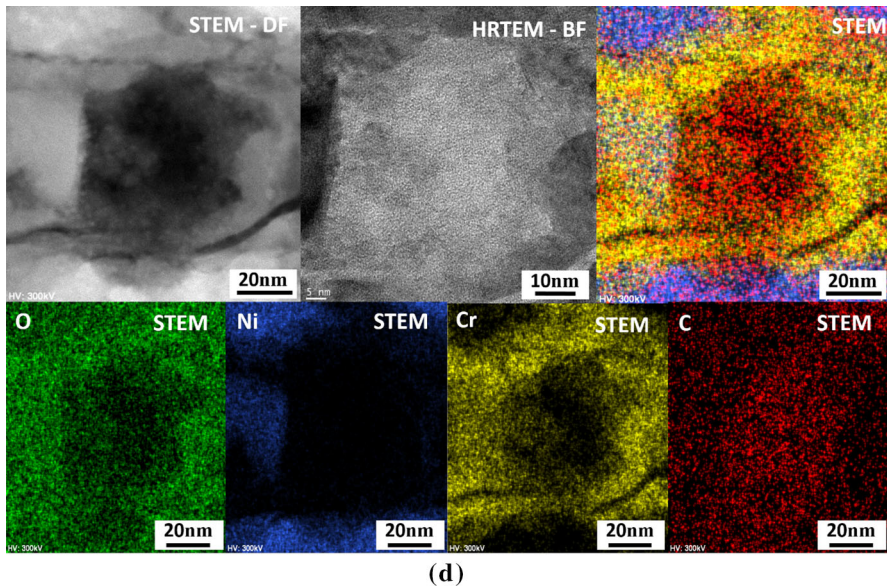
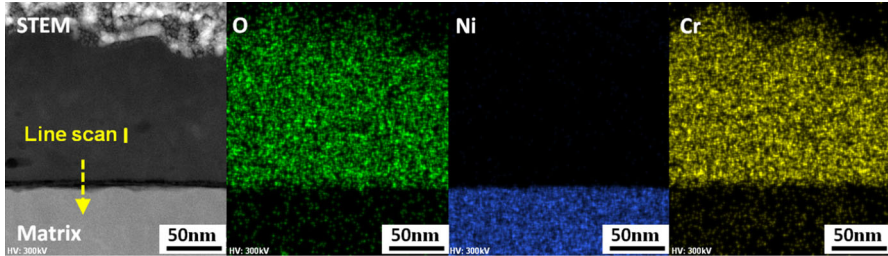


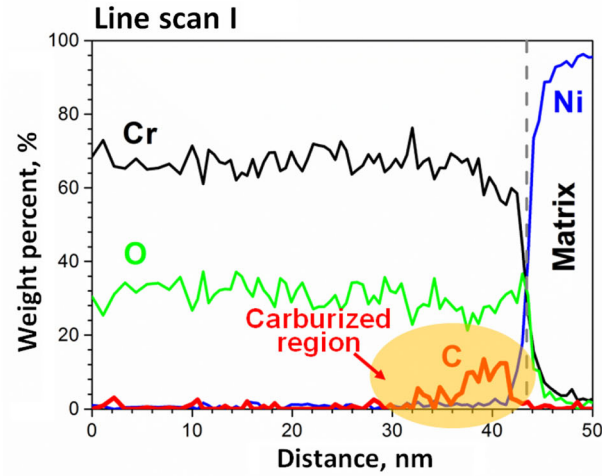
Fig. 4 continued

is in agreement with the XRD results (Fig. 2). Similar results were previously reported for Ni–Cr binary alloys exposed in Ar-20CO₂ environment, such that the NiCr₂O₄ spinel was absent at 650 °C [15], but present at slightly higher temperature of 700 °C [16]. EDS line scanning showed the almost complete depletion of Cr in the matrix directly beneath the chromia layer on Ni-7Cr binary alloy (Fig. 4c), which is in agreement with the observation that the upper part of inner layer is predominantly Cr₂O₃ while lower part of inner layer is predominantly NiO. Interestingly, the presence of C layer was detected in the upper part of inner oxide layer where Cr₂O₃ was dominant (Fig. 4b), while C enrichment was not shown in the lower part of inner oxide layer where NiO was dominant (Fig. 4c). Further, the presence of dark regions throughout the internal oxide from STEM dark field mode revealed out to be a lump of non-diffracting, amorphous region within the regular oxide lattice from high-resolution bright field mode as shown in Fig. 4d. The STEM-EDS mapping in Fig. 4d showed that such regions were enriched with C encircled by inner chromia layer, similar to the amorphous C region previously observed in chromia-forming alloys [11]. The probable mechanism will be discussed in the following section.

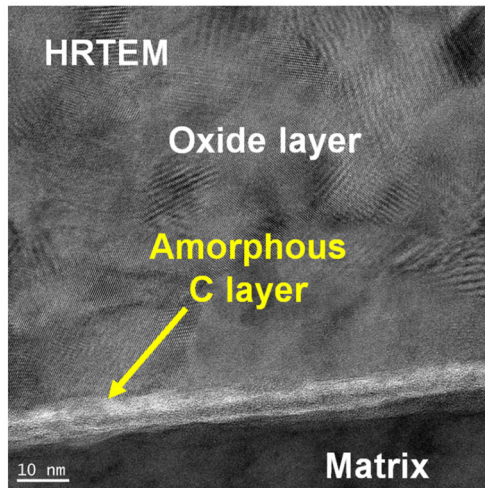
For alloys with higher Cr content (greater than 14% Cr), a thin and continuous chromia layer was observed (Figs. 5, 6) with an average oxide thickness of around



(a)



(b)



(c)

Fig. 5 TEM analyses results of oxide layer on Ni-14Cr binary alloy corroded in S-CO₂ at 600 °C (20 MPa) for 200 h. **a** Cross-sectional STEM micrograph and EDS mapping images, **b** line scan at the matrix–oxide interface and **c** HRTEM micrograph highlighting the amorphous C layer

130–150 nm. The reduced corrosion rate in chromia-forming alloys could be attributed to the formation of initial protective chromia layer, while Ni-7Cr binary alloy failed to form protective chromia due to the insufficient Cr content, resulting in the poorest corrosion resistance (Figs. 1, 2). Therefore, it could be said that the minimum Cr content for continuous chromia formation in 600 °C S-CO₂ environment would be between 7 and 14%. Once Cr content in Ni-*x*Cr binary alloys was enough for continuous chromia formation, the change in corrosion rate was rather small as in Fig. 2.

EDS line scanning results showed the depletion of Cr in the matrix directly beneath the chromia layer for Ni-14Cr binary alloy (Fig. 5b), while the degree of Cr depletion was not significant for Ni-22Cr binary alloy (Fig. 6b). The presence of Cr-

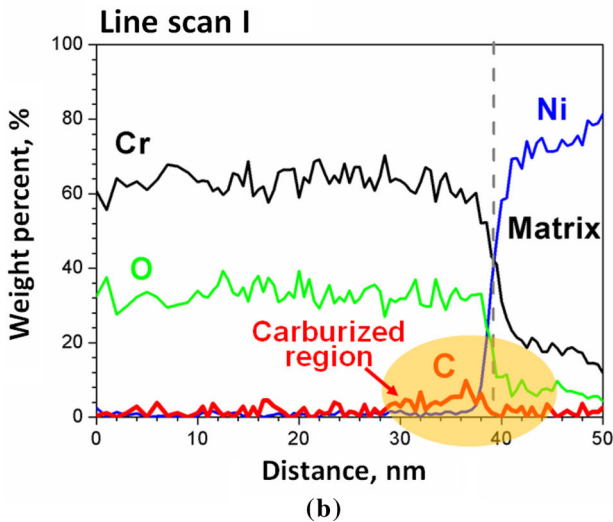
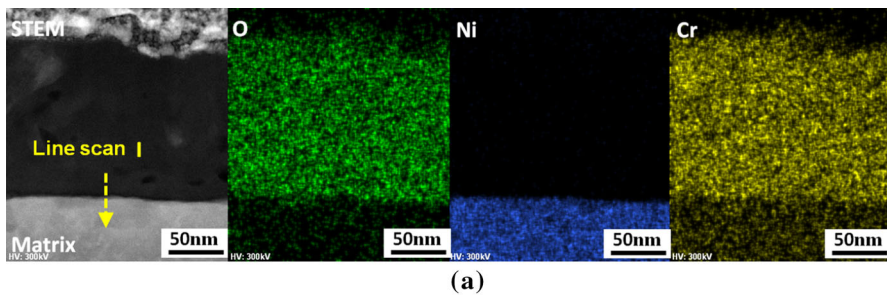


Fig. 6 TEM analyses results of oxide layer on Ni-22Cr binary alloy corroded in S-CO₂ at 600 °C (20 MPa) for 200 h. **a** Cross-sectional STEM micrograph and EDS mapping images and **b** line scan at the matrix–oxide interface

depleted zone beneath the oxide layer for Ni- x Cr binary alloys suggests that Cr would diffuse outwards from the matrix and be oxidized at the oxide–matrix interface [17]. Despite the severe Cr depletion below the chromia layer for Ni-14Cr binary alloy, NiO layer was not observed from STEM-EDS analyses (Fig. 5), which suggest the slow but stable growth of chromia layer could be supported by the outward diffusion of Cr from the underlying matrix. Previously, the stable growth of chromia layer despite the Cr depletion in the matrix was reported for Alloy 600 (16% Cr) exposed up to 1000 h at the same environment [11]. That is, the Ni and Cr oxides formed by the inward diffusion of oxygen, which was observed for the Ni-7Cr alloys, were not observed for alloys with more than 14% Cr. However, a recent similar study of Ni–Cr binary alloys in Ar-20CO₂ environment at 650 °C showed continuous chromia was formed only when Cr content reached 30 wt%. In that case, the Ni–Cr binary alloys formed external NiO with an internal mixture of NiO and Cr₂O₃ layer, in which the internal layer was predominated by Cr₂O₃ on higher Cr content. Such distinct phenomena were observed because of their preceding electroplating procedure, which removed work hardened or deformed layer in the surface, thereby preventing enhanced diffusion of alloying elements towards the surface. Moreover, no such procedures were carried out in this study, which enabled rapid Cr-diffusion onto the surface to form continuous chromia even with the Cr content of 14 wt%.

Meanwhile, EDS line scanning results consistently showed the presence of C layer, despite the formation of continuous chromia layer for alloys with higher Cr content (greater than 14% Cr). On the other hand, C layer was not observed for pure Ni on which NiO was formed (Fig. 3). Previously, the carburized region at the interface between outer chromia layer and matrix was identified as amorphous C layer, which was confirmed by the lack of ordered atomic arrangement in high-resolution TEM image [11] as shown in Fig. 5c. The presence of amorphous C layer below the seemingly protective chromia layer has puzzled authors since the observation of such behaviours for several heat-resistant austenitic alloys [11, 12]. In the following section, authors tried to understand the mechanism behind the formation of C layer below chromia layer in S-CO₂ environment.

Carburization in S-CO₂ Environment

As mentioned in the previous section, carbon-enriched (10 wt%) region was observed at the oxide–matrix interface from the STEM-EDS line scanning of Ni-14Cr and Ni-22Cr binary alloys as shown in Figs. 5b and 6b. Meanwhile, a small amount C was detected for Ni-7Cr binary alloy directly beneath the chromia layer (Fig. 4b), while C was practically not observed beneath the NiO layer (Fig. 4c). SIMS analysis was performed to qualitatively check C concentration in the oxide layer and C penetration into the matrix, and the results are shown in Fig. 7. Based on SIMS results, C layer was absent beneath the oxide layer for pure Ni and very small amount of C layer was observed within the oxide layer for Ni-7Cr alloy. Meanwhile, the presence of C layer was clearly detected below the oxide layer for Ni- x Cr binary alloys with more than 14% of Cr on which chromia layer was formed. Despite the presence of C layer at the oxide–matrix interface, no carbide precipitates

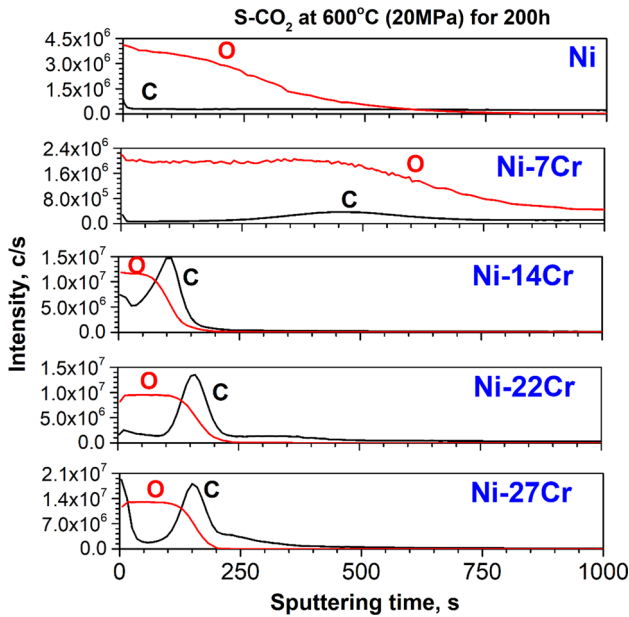


Fig. 7 SIMS depth profile of C and O from oxide layer in S-CO₂ at 600 °C (20 MPa) for 200 h

were observed in the underlying matrix in all binary alloys, in agreement with the behaviour observed for the commercial chromia-forming Ni-based Alloy 600 and Alloy 690 [11].

The carburization mechanism for the chromia-forming alloys could be described as follows. First, CO₂ dissociates at high temperature into CO and O₂ according to the following reaction:



It has been reported that carbonaceous species would penetrate the oxide layer through the high-diffusion paths such as nano-channels, pores, cracks or grain boundaries [18–20] and dissociate to induce corrosion and carburization via the following reactions [21]:



where M is Cr or Ni; x, y = 1 for Ni; and x = 2, y = 3 for Cr. This is followed by C deposition at the oxide–matrix interface by Boudouard reaction [22]:



However, the absence of amorphous C layer in pure Ni could not be explained by above mechanism. The probable difficulty in transport of carbonaceous species through NiO could not be the reason since a minute amount of C deposition has been observed for Ni-7Cr binary alloy having NiO in the outer layer (Fig. 4b). Therefore, other factors have to be considered in the C deposition process.

Gheno et al. [23] reported that the local C activity (a_C) at the oxide–matrix interface depended directly on the local equilibrium oxygen partial pressure $(pO_2)_{eq}$ when equilibrium condition was achieved at the oxide–matrix interface for CO_2 , CO and O_2 . The equilibrium condition for the reactions (1) and (3) can be expressed by the following equations:

$$\frac{pCO}{pCO_2} = \frac{K_2}{(pO_2)_{eq}^{1/2}} \quad (4)$$

$$a_C = K_4 \frac{(pCO)^2}{pCO_2}, \quad (5)$$

where K_2 and K_4 represent the equilibrium constant for reactions (1) and (3), respectively. According to above equations, the lower the $(pO_2)_{eq}$ the higher the a_C would be, which favours the deposition of C. The previous attempt to quantitatively determine the formation of C layer based on the estimation of a_C using above equations was not successful for chromia as the supply of CO and CO_2 to the interface was not enough to support the equilibrium [23, 24]. Nonetheless, above equations can be used to qualitatively compare the a_C of different oxides such as Cr_2O_3 and NiO to explain the presence and absence of C layer at the interface.

The equilibrium reactions for Ni–Cr binary alloy system with O_2 are given by:



The $(pO_2)_{eq}$ at the oxide–matrix interface is equal to that of dissociation pressure of the corresponding oxide in oxide–metal equilibrium. The values were calculated from the oxide phase equilibrium diagram at 600 °C using Thermo-Calc[®] software [25]. It was calculated that $(pO_2)_{eq}$ for Cr_2O_3 (corundum)–metal equilibrium was in the order of 10^{-36} atm, while for NiO (Halite)–metal equilibrium, it was in the order of 10^{-20} atm, significantly greater than that for chromia. Therefore, high $(pO_2)_{eq}$ for NiO –metal equilibrium resulted in lower a_C at the interface, which would make the accumulation of C difficult in pure Ni. Meanwhile, much higher a_C for chromia could explain the formation of amorphous C layer in chromia-forming Ni–xCr binary alloys with more than 14% of Cr. In addition, the presence of small amount of C deposition within the oxide layer on Ni–7Cr binary alloy could be explained in view of the oxide structure. As shown in Fig. 4, the chromia was mostly embedded within the predominant NiO in the inner oxide layer and was located some distance away from the oxide–matrix interface. Therefore, due to the high $(pO_2)_{eq}$ for the $NiO + Cr_2O_3$, C deposition was not expected. However, in some isolated locations where the chromia was in direct contact with matrix during its growth, the low enough $(pO_2)_{eq}$ and high a_C condition was achieved and C deposition happened locally. Then, due to the sparse Cr content in the matrix, discontinuous inner layer chromia was developed, which resulted in deposition of C along the irregular

chromia–matrix interface during its growth. Further ingress of carbonaceous species would have oxidized adjacently situated Ni-rich matrix without any C deposition. As a result, C deposition was possible along the chromia interface for Ni–7Cr binary alloy as shown in Fig. 4b, d.

Also in a recent report, intergranular carbides observed in Ni–Cr binary alloy containing above 25 wt% Cr were attributed to higher a_C arising from predominant chromia on the surface [15]. However in this study, despite the formation of amorphous C layer at the oxide–matrix interface for chromia-forming Ni–xCr binary alloys with more than 14% of Cr, further diffusion of C into the matrix and the formation of Cr-carbides were not observed by cross-sectional SEM images, which are not shown. Previously, it has been reported that the C at the interface would diffuse into the matrix and form carbides by combining with the available Cr for Fe-based alloys [9, 11, 23]. On the other hand, the underlying matrix was not affected by the presence of C layer for other Ni-based alloys like Alloy 600 and Alloy 690 [11, 12], which is in agreement with the current observation.

The carbon activity, a_C , at the interface and the corresponding C diffusion into the matrix should be also considered regarding the matrix carbide precipitation. The a_C required to precipitate carbides in Ni–xCr binary alloys at 600 °C was calculated by Thermo-Calc software, and the results are shown in Fig. 8. It could be said that carbide precipitation is thermodynamically possible in Ni–xCr binary alloys provided sufficient C and Cr are present in the matrix. The carbide formation is thermodynamically not favourable when the Cr content drops below the lower limit around 6% even when sufficient C is present as in the oxide–matrix interface. However, the lower C concentration in the matrix would require more Cr to form carbides, which was not the case when Cr was depleted in the matrix below the oxide layer as observed in Figs. 5 and 6. Therefore, for chromia-forming Ni–xCr binary alloys and commercial Ni-based alloys like Alloy 600, the a_C at the interface of the inner chromia and matrix would be enough to deposit C there but insufficient

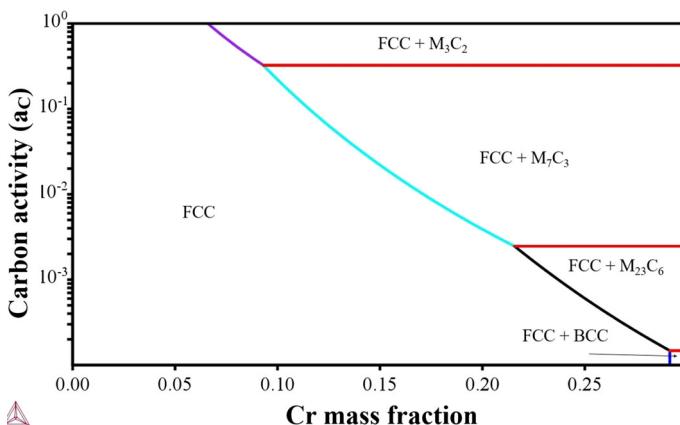


Fig. 8 Carbide stability diagram as the function of Cr content in Ni–xCr binary alloy at 600 °C as calculated by Thermo-Calc software

to precipitate carbides in the underlying matrix in high-temperature S-CO₂ environment.

Conclusions

Corrosion and carburization behaviour of pure Ni and Ni-*x*Cr (*x* = 7, 14, 22 and 27 wt%) binary alloys in high-temperature S-CO₂ environment was investigated. Specimens were exposed to S-CO₂ environment at 600 °C and 20 MPa for 200 h. Based on the tests and subsequent analysis, the following conclusions were drawn:

1. For pure Ni, a continuous NiO layer was developed. Meanwhile, a relatively thin and continuous chromia (Cr₂O₃) was formed on alloys containing at least 14% Cr, resulting in better corrosion resistance. In addition, the corrosion resistance was about the same for the alloys with at least 14% Cr, whereas Ni-7Cr binary alloy showed the poorest corrosion resistance with a complex oxide structure consisted of outer uniform NiO layer and inner layer of a rather irregular Cr₂O₃ mixed with NiO.
2. Despite good corrosion resistance, the presence of C layer was detected below the chromia layer for Ni-*x*Cr binary alloys containing at least 14% Cr, while C layer was not present for pure Ni with NiO layer. Meanwhile, for the Ni-7Cr binary alloy, amorphous C regions were present throughout the inner layer encircled with chromia.
3. Thermodynamic calculation was used to explain the formation of C layer below chromia layer. The low (pO₂)_{eq} for chromia–matrix interface resulted in higher carbon activity, which was in agreement with the presence of C layer below chromia layer. On the other hand, high (pO₂)_{eq} for NiO–matrix interface resulted in lower carbon activity, which explained the absence of C layer below NiO.

Acknowledgements This study was partly supported by the Engineering Research Center Program of MSIP/NRF (No. 2016R1A5A1013919), the Nuclear R&D program of MOTIE/KETEP of Korea (No. 20161110100120) and the Korea Institute of Materials Science (KIMS). Financial support for two of the authors is provided by the BK-Plus Program of the MSIP of Korea.

References

1. E. J. Parma, S. A. Wright, M. E. Vernon, D. D. Fleming, G. E. Rochau, A. J. Suo-Anttila, A. A. Rashdan, P. V. Tsvetkov, *Supercritical CO₂ direct cycle gas fast reactor (SC-GFR) concept*, Sandia National Laboratory Report 2011 SAND2011-2525.
2. Y. Ahn, S. J. Bae, M. Kim, S. K. Cho, S. Baik, J. I. Lee and J. E. Cha, Review of supercritical CO₂ power cycle technology and current status of research and development. *Nuclear Engineering and Technology* **47**, 647 (2015).
3. H. C. No, J. H. Eoh, Y. H. Yoo and S. O. Kim, Sodium-CO₂ interaction in a supercritical CO₂ power conversion system coupled with a sodium fast reactor. *Nuclear Technology* **173**, 99 (2011).
4. B. D. Iverson, T. M. Conboy, J. J. Pasch and A. M. Kruizenga, Supercritical CO₂ Brayton cycles for solar-thermal energy. *Applied Energy* **111**, 957 (2013).

5. H. Chen, D. Y. Goswami and E. K. Stefanakos, A review of thermodynamic cycles and working fluids for the conversion of low-grade heat. *Renewable and Sustainable Energy Reviews* **14**, 3059 (2010).
6. T. Dixon, K. Yamaji, R. J. Allam, M. R. Palmer, G. W. Brown, J. Fetvedt, D. Freed, H. Nomoto, M. Itoh, N. Okita and C. Jones, High efficiency and low cost of electricity generation from fossil fuels while eliminating atmospheric emissions, including carbon dioxide. *Energy Procedia* **37**, 1135 (2013).
7. T. Furukawa, Y. Inagaki and M. Aritomi, Compatibility of FBR structural materials with supercritical carbon dioxide. *Progress in Nuclear Energy* **53**, 1050 (2011).
8. F. Rouillard, F. Charton and G. Moine, Corrosion behavior of different metallic materials in supercritical carbon dioxide at 550 °C and 250 bars. *Corrosion* **67**, 095001 (2011).
9. G. Cao, V. Firouzdor, K. Sridharan, M. Anderson and T. R. Allen, Corrosion of austenitic alloys in high temperature supercritical carbon dioxide. *Corrosion Science* **60**, 246 (2012).
10. V. Firouzdor, K. Sridharan, G. Cao, M. Anderson and T. R. Allen, Corrosion of a stainless steel and nickel-based alloys in high temperature supercritical carbon dioxide environment. *Corrosion Science* **69**, 281 (2013).
11. H. J. Lee, H. Kim, S. H. Kim and C. Jang, Corrosion and carburization behavior of chromia-forming heat resistant alloys in a high-temperature supercritical-carbon dioxide environment. *Corrosion Science* **99**, 227 (2015).
12. H. J. Lee, G. Obulan Subramanian, S. H. Kim and C. Jang, Effect of CO₂ pressure on corrosion and carburization behavior of chromia-forming alloys in high temperature supercritical-carbon dioxide environment. *Corrosion Science* **111**, 649 (2016).
13. H. J. Lee, S. H. Kim, H. Kim and C. Jang, Corrosion and carburization behavior of Al-rich surface layer on Ni-base alloy in supercritical-carbon dioxide environment. *Applied Surface Science* **488**, 483 (2016).
14. H. V. Atkinson, A review of the role of short-circuit diffusion in the oxidation of nickel, chromium, and nickel-chromium alloys. *Oxidation of Metals* **24**, 177 (1985).
15. Y. Xie, J. Zhang and D. J. Young, Temperature Effect on Oxidation Behavior of Ni-Cr Alloys in CO₂ Gas Atmosphere. *Journal of The Electrochemical Society* **164**, C285 (2017).
16. T. D. Nguyen, Y. Xie, S. Ding, J. Zhang and D. J. Young, Oxidation Behavior of Ni–Cr Alloys in CO₂ at 700 °C. *Oxidation of Metals* **87**, 605 (2017).
17. F. Hamdani, H. Abe, B. Ter-Ovanesian, B. Normand and Y. Watanabe, Effect of chromium content on the oxidation behavior of Ni-Cr model alloys in superheated steam. *Metallurgical and Materials Transactions A* **46**, 2285 (2015).
18. J. A. Colwell and R. A. Rapp, Reactions of Fe-Cr and Ni-Cr alloys in CO/CO₂ gases at 850 and 950 °C. *Metallurgical Transactions A* **17**, 1065 (1986).
19. I. Wolf, H. J. Grabke and P. Schmidt, Carbon transport through oxide scales on Fe–Cr alloys. *Oxidation of Metals* **29**, 289 (1988).
20. D. J. Young, T. D. Nguyen, P. Felfer, J. Zhang and J. M. Cairney, Penetration of protective chromia scales by carbon. *Scripta Materialia* **77**, 29 (2014).
21. F. Rouillard and T. Furukawa, Corrosion of 9–12Cr ferritic–martensitic steels in high-temperature CO₂. *Corrosion Science* **105**, 120 (2016).
22. J. E. Antill and J. B. Warburton, Behaviour of carbon during the corrosion of stainless steel by carbon dioxide. *Corrosion Science* **7**, 645 (1967).
23. T. Gheno, D. Monceau, J. Zhang and D. J. Young, Carburisation of ferritic Fe–Cr alloys by low carbon activity gases. *Corrosion Science* **53**, 2767 (2011).
24. C. S. Giggins and F. S. Pettit, Corrosion of metals and alloys in mixed gas environments at elevated temperatures. *Oxidation of Metals* **14**, 363 (1980).
25. J.-O. Andersson, T. Helander, L. Höglund, P. Shi and B. Sundman, Thermo-Calc & DICTRA, computational tools for materials science. *Calphad* **26**, 273 (2002).